

A verification procedure for environmental acoustic codes

presented at the Congrès Français d'Acoustique 2018 - Le Havre (France)

Pierre ChobEAU¹ and Judicaël Picaut²

¹LAUM, CNRS UMR 6613, Le Mans Université, avenue Olivier Messiaen, F-72085 Le Mans, France

²IFSTTAR, UMRAE, Route de Bouaye, F-44344 Bouguenais, France

A verification procedure based on grid convergence study is proposed for the verification of environmental acoustic codes. Analytical solutions of five test cases - *i.e.* 2D acoustic geometrical scenes - are used for the error calculation. The errors are presented using the two-norm and the max-norm, and shown as a function of the spatial step. The observed order of accuracy is also presented for each numerical method and each test case. Most cases show a second order convergence rate as expected from the theory. Depending on the method and the test case, convergence rates and observed orders of accuracy are prone to fluctuations. All codes used here are available online (written using Python programming language 2.7.14) and this project is open for contribution.

1 Introduction

With a steady increase of available numerical resources, computational methods, such as wave based methods, applied to outdoor acoustics allow for long range sound propagation within an acceptable frequency range. However, before simulating complete acoustic scenes, the codes have to be thoroughly verified and validated. This can be carried out using specific Verification and Validation (V&V) procedures [1, 2].

The verification procedure consists in the comparison of the numerical results with analytic solutions that are mainly available for basic geometries. This can be achieved by checking the accuracy of the results for each physical phenomena that takes place in outdoor acoustics *e.g.* ground reflection, diffraction by edges, meteorological effects... Once the verification procedure has been performed, more complexity can be added into the acoustic scenes, *e.g.* including irregular geometries, heterogeneous media, in order to get closer to real cases. Analytic solution are usually not available for these complex scenes, therefore in these cases the numerical results are compared with experimental data. This procedure is called validation. Both verification and validation require the definition of benchmark test cases that define the geometries and all parameters describing the acoustic propagation.

Benchmark test cases for outdoor sound propagation has first been introduced in the mid ninety's by Attenborough *et. al* [3], in which the Fast Field Program (FFP) and the Parabolic Equation (PE) are compared to analytical solutions for sound propagation above impedance grounds in presence of four types of meteorological conditions. More recently, an online platform benchmark has been released [4], in which four fields of acoustics are represented. The website provides examples of benchmark definitions, including geometries and numerical setups for each case. However, none of these references provide a detailed procedure for the verification of acoustic codes.

The main contribution of this communication is the presentation and the application of a detailed verification procedure for outdoor acoustic codes in either time or frequency domain. A brief reminder on error and norms calculation is presented in Section 2. Section 3 gives the five main steps that can be followed to carry out a code verification procedure. In Section 4, this procedure is applied on five geometrical test cases, where the numerical results are given using convergence rates and orders of accuracy. Ultimately, this work might give rise to an online platform aiming for the verification of environmental acoustic codes.

2 Error and norms calculations

The present section is mainly based on [5, App.A, p.245-258]. The variables for the integrations and error measures on the acoustic pressure have been adapted to two-dimensional (2D) time-domain methods.

The absolute error between a numerical solution \hat{p}_i^n calculated with a time domain method (FDTD, TLM...) at a given location $(0, x, y)$ and at the time t can be defined as

$$\text{error}(x_i, y_i, t_n) = \left| \hat{p}_i^n - p_{(x,y,t)}^{\text{exact}} \right|. \quad (1)$$

where $p_{(x,y,z,t)}^{\text{exact}}$ is the exact pressure that can be derived, for basic cases, as analytical solutions. The coordinates x_i and y_i are the discrete location on the numerical grid, and t_n is the discrete time sequence.

The magnitude of the error can be measured using standard function space norm for a given time iteration t_n that can be expressed for the general q -norm as

$$\|\text{error}\|_q = \left(\int_{x,y} |\text{error}(x, y, t = t_n)|^q dx dy \right)^{1/q}. \quad (2)$$

For a discrete numerical grid application, Eq. (2) can be rewritten in a discrete form as

$$\|\text{error}\|_q = \left(\sum_{i,j} |\text{error}_{i,j}^n|^q h^2 \right)^{1/q}, \quad (3)$$

where h is the spatial step, n is the discrete time iteration and the subscripts i, j are the discrete coordinates on the numerical grid.

Similarly, in the frequency domain it becomes

$$\|\text{ERROR}\|_q = \left(\sum_{i,j} |\text{ERROR}_{i,j}^{f_n}|^q h^2 \right)^{1/q}, \quad (4)$$

where the ERROR is now calculated for a given frequency f_n from pressure signals obtained using frequency domain methods.

Another way to look at the convergence rate is to show the observed order of accuracy that corresponds to the measured convergence rate between two grids. The observed order of accuracy p between two consecutive spatial steps h_1 and h_2 can be expressed as

$$p_{\text{obs.}} = \frac{\log_{10}(\|\text{error}\|_q(h_1)/\|\text{error}\|_q(h_2))}{\log_{10}(h_1/h_2)}. \quad (5)$$

where $h_1 - h_2$ has to be small enough such as explained in [5].

In the results Sec. 4, the norms are calculated using the function `numpy.linalg.norm` from the package **numpy** [6] used for scientific computing with Python [7] programming language 2.7.14.

3 Code verification procedure

Considering a given numerical method applied on a given geometrical test case, the verification procedure can be carried out following these five main steps :

1. implementation of the analytical source term in the numerical method (initial condition), or use of a well known source signal - *e.g.* Gaussian pulse,
2. comparison between the numerical results and the analytical solution in time or frequency domain, which gives the absolute error (see Eq. (1)),
3. repetition of step 2 for at least five spatial steps (h_1 to h_N) that corresponds to five Cartesian grid spacing,
4. calculation of the spatial norm of the error Eq. (3) or Eq. (4) for each grid,
5. presentation of the convergence rate - *e.g.* using *log-log* plots, and calculation of the observed order of accuracy (see Eq. (5)).

These steps can be applied to either time or frequency domain numerical methods as shown in the following section.

4 The five test cases used for code verification

The three numerical codes that are going to be verified in this document are based on the three following methods : the finite difference applied to the Helmholtz (FDH) equation [8], the finite difference time domain (FDTD) method [9] and the transmission line matrix (TLM) method [10, 11]. Their principle is not given here for the sake brevity. It is worth mentioning, that all methods use standard rectilinear grids - *i.e.* aligned and evenly spaced nodes networks.

Five test cases made of basic geometrical 2D scenes are used for the following codes verifications. These cases allow for the test of outdoor acoustics phenomena such as free field propagation in case 2, reflecting boundary conditions from street canyons or rectangular courtyards in case 3, ground reflection in case 4, acoustic diffraction by circular obstacles such as tree trunks in case 5. The five respective ‘exact’ solutions are calculated analytically.

Based on the local truncation error found for second order propagation equations discretized using centered finite differences - see *e.g.* [9, Sec. II.F.] - the expected convergence rate for the three numerical methods is of second order.

4.1 Case 1 : Laplace operator eigenfunction

4.1.1 Formulation

This test case corresponds to the sampled eigenfunction of the Laplace operator [12] that is written as

$$\hat{P}_{i,j} = \sin(\pi i h/L_x) \sin(\pi j h/L_y), \quad (6)$$

where L_x and L_y are the lengths of the domain. Here $L_x = L_y = L = 1$ m. This gives the source function

$$\hat{F}_{i,j} = \left(\frac{3\pi^2}{L^2} + k^2 \right) \sin(\pi i h/L) \sin(\pi j h/L). \quad (7)$$

4.1.2 Numerical setup

The source term defined by Eq. (7) is implemented into the numerical update of the FDH method. The numerical domain is a square of 1 m side lengths. It is discretized using a regular rectilinear grid of nodes. A total of 50 grid sizes are used with a spatial step ranging from $h_1=0.001$ m to $h_{50}=0.1$ m. The error is calculated for each grid using Eq. (6) as a reference for the analytic form of the pressure.

4.1.3 Results

The pressure field inside the numerical domain of the FDH method is depicted in Figure 1.

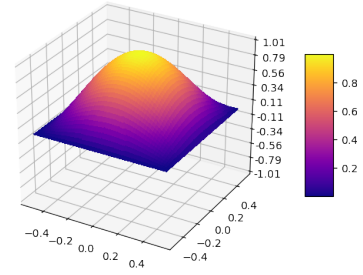


FIGURE 1 – Real part of the normalized pressure obtained using the FDH method.

The error defined by Eq. (1) is the absolute value of the difference between the numerical result and the analytic formulation (6). The norms of the error are calculated over all grid points for each spatial step. Figure 2 shows the two-norm and the max-norm of the errors. The second order convergence rate is observed for max-norm, whereas the two-norm shows a 2.5 convergence order. This 2.5 convergence remains to be explained, as the expected rate is around 2. As expected, the observed orders of accuracy start fluctuating around the formal order of convergence when the grids get coarser.

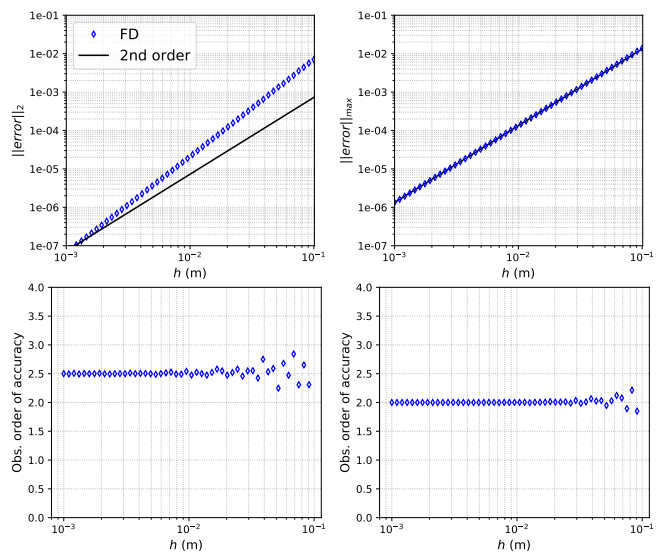


FIGURE 2 – Two-norm and max-norm of the absolute error (top) and the corresponding observed orders of accuracy (bottom) for case 1, using the FDH method.

4.2 Case 2 : geometrical spreading of a 2D point source

Case 2 is used for time domain methods - here FDTD or TLM - since the numerical time signals are directly comparable to the following pulse formulation.

4.2.1 Formulation

The Gaussian pulse used as a source signal at the node i is written as

$$\hat{f}_i^n = \exp\left(-\pi^2 (0.5fnT_s - 1)^2\right), \quad (8)$$

where f is the maximal frequency, T_s the time step and n is an integer that corresponds to the time iteration. The magnitude of this 2D point source theoretically decays proportionally to the inverse square root of the distance between the source and the receiver. Therefore, the analytic formulation of the signal can be rewritten as

$$\hat{f}_i^n = 1/\sqrt{d_{sr}} \exp\left(-\pi^2 (0.5f(nT_s - d_{sr}/c) - 1)^2\right), \quad (9)$$

where d_{sr} is distance between the source and the receiver.

4.2.2 Numerical setup

The numerical domain is simply made of a point source located at its center. The receivers are located on two axes, one following the axis of the numerical network, one following the diagonal. The numerical domain is a 2D rectilinear network, in which a point source located at the center emits the Gaussian pulse defined by Eq. (8) with a cutoff frequency of 2000 Hz.

Figure 3 shows the receiver locations - one every 0.5 m on each axis, axial and diagonal. The simulation duration is $T = 20$ ms, so no unwanted reflection from the limit of the domain can reach the receivers. The spatial steps used for the following grid convergence study are (from finest to coarsest) $h = [0.01, 0.02, 0.04, 0.08, 0.16]$ m. The corresponding time steps for each grid are set equal to $T_s = [0.125, 0.25, 0.50, 1.00, 2.00] \cdot 10^{-4}$ s. It is important to note that the grid parameters have been chosen to be exact multiple from one grid to another in order to accurately compare the grids both in terms of time iteration and receiver position. Therefore, the simulations are carried out below the theoretical Courant limit, *i.e.* $\lambda = cT_s/h < 1/\sqrt{2}$.

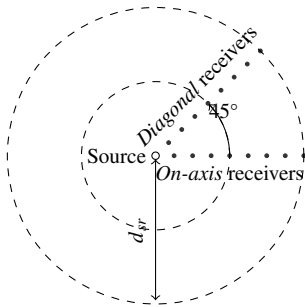


FIGURE 3 – Geometry of the case 2 : the maximal distance between the source and the receiver is $d_{sr} = 4$ m, with 8 receivers per axis.

4.2.3 Results

The errors are the averaged difference between the numerical time signals and the analytical formulation (9). The norms are calculated over all receivers. Both methods shows second order of convergence, as shown in Figure 4. The TLM convergence appears to be more impacted than FDTD for the coarsest grids, where the order of convergence is reduced.

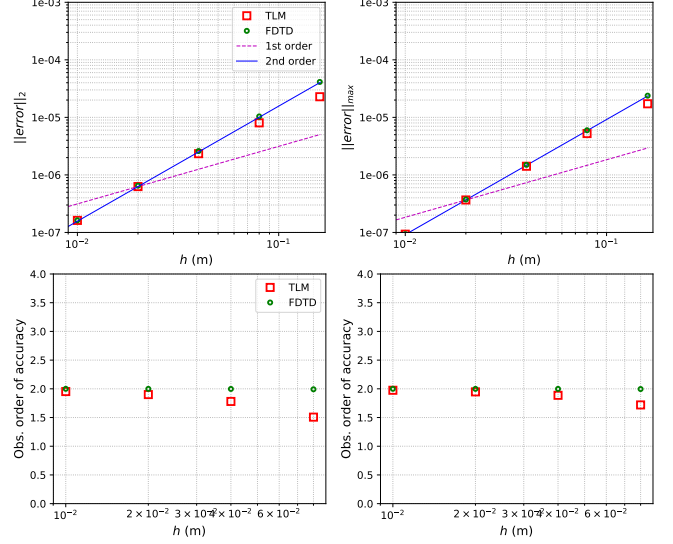


FIGURE 4 – Two-norm and max-norm of the absolute error (top) and the corresponding observed orders of accuracy (bottom) for case 2, using the FDTD and the TLM methods.

4.3 Case 3 : acoustic modes of a 2D rectangular domain

4.3.1 Formulation

Case 3 aims at testing the reflecting boundary condition of a 2D rectangular closed domain. The exact solution of such a setup at the iteration n is written as

$$p_{\text{exact}}(i, j, n) = \cos\left(\frac{n_i \pi i}{L_i}\right) \cos\left(\frac{n_j \pi j}{L_j}\right) \cos(\omega_{i,j} n \delta t), \quad (10)$$

where

$$\omega_{i,j} = \pi c \sqrt{\left(\frac{n_i}{L_i}\right)^2 + \left(\frac{n_j}{L_j}\right)^2}, \quad (11)$$

where i, j are the discrete node location on the grid, n_i and n_j are the modes numbers. The exact solution (10) is used as an initial condition and imposed at each point of the domain at the first time step.

4.3.2 Numerical setup

The rectangular domain is of side lengths $L_x = 2.36$ m \times $L_y = 1.28$ m. The spatial steps h and the time steps T_s used for the grids are identical to case 2.

The two modes studied in this test are shown in Figure 5 for an FDTD simulation. From this pressure rendering, the FDTD simulations seem to be in good agreement with the analytic solutions.

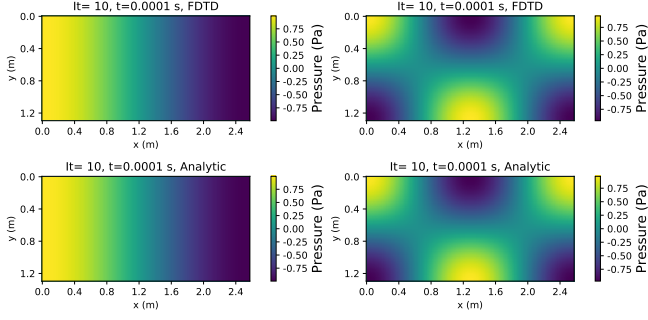


FIGURE 5 – Snapshots of the pressure returned by the FDTD update inside the 2D rectangular domain using the finest grid ($h = 0.01$ m and $T_s = 0.125 \cdot 10^{-4}$ s) for the modes : (a) $n_x = 1$, $n_y = 0$; (b) $n_x = 2$, $n_y = 1$.

4.3.3 Results

Figure 6 shows the norms of the errors for the three numerical methods. All are second order convergent as expected from the local truncation error - see *e.g.* [9, Sec. II.F.].

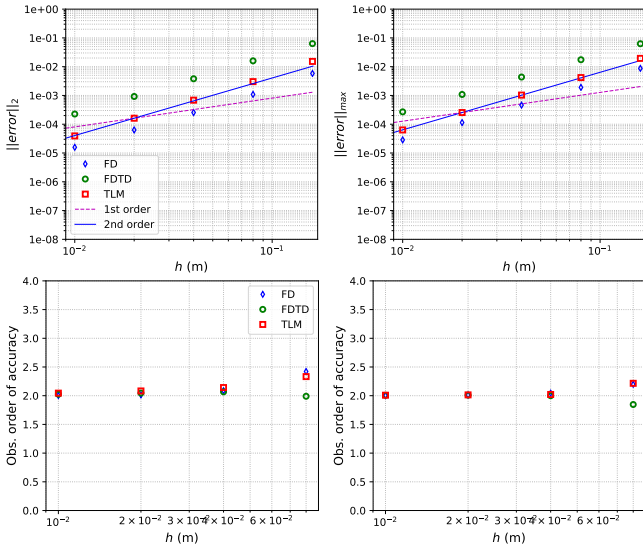


FIGURE 6 – Two-norm and the max-norm of the absolute error (top) and the corresponding observed orders of accuracy (bottom) for case 3, using the FDH, the FDTD and TLM methods.

It can be noted that, this case can be used with both time domain methods - using initial condition, and frequency domain methods - assuming the harmonic behavior of the exact solution, *i.e.* $\omega_{i,j} n \delta t = 0$ in Eq. (10). However, it only takes into account perfectly reflecting boundary conditions.

4.4 Case 4 : reflection from a ground

4.4.1 Formulation

The analytic solution for this case can be found in [13]. The total pressure field p_{total} that takes into account both the direct and reflected waves that respectively follow the paths R_1 and R_2 can be written as

$$p_{\text{total}} = \frac{e^{jkR_1}}{R_1} + Q \frac{e^{jkR_2}}{R_2}, \quad (12)$$

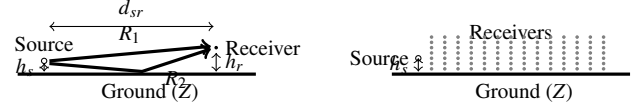


FIGURE 7 – Geometry of the case 4 (left) with $h_s = 0.64$ m, $d_{sr} = [0.32 : 0.32 : 5.12]$ m and $h_r = [0.32 : 0.32 : 2.24]$ m ; depiction of the receiver grid (right) with a total of 112 receivers.

where k is the wave number and Q is given by

$$Q = R_p + (1 - R_p)F_w, \quad (13)$$

where R_p is the reflection coefficient written as

$$R_p = \frac{\cos(\theta) - 1/Z}{\cos(\theta) + 1/Z}, \quad (14)$$

and F_w can be written as

$$F_w = 1 + J \sqrt{\pi} w e^{-w^2} \text{erfc}(-jw). \quad (15)$$

and

$$w = \frac{1 + j}{2} \sqrt{kR_2} \left(\cos(\theta) + \frac{1}{Z} \right), \quad (16)$$

where Z is the surface impedance of the ground and θ the angle between the axis normal to the ground and the reflected path.

4.4.2 Numerical setup

Case 4 is the study of a point source emitting a Gaussian pulse above a perfectly reflecting ground as depicted in Figure 7. The source height is $h_s = 1.50$ m. The receivers are located on the grids with an horizontal spacing of 0.5 m - *i.e.* between $d_{sr} = 0.5$ m and $d_{sr} = 7.0$ m and a vertical spacing of 0.2 m - *i.e.* between $h_r = 0.2$ m and $h_r = 1.4$ m. The spatial steps h and the time steps T_s used for the grids are identical to case 2.

4.4.3 Results

The attenuation as a function of frequency for the TLM, the FDTD and the analytic solutions are shown in Figure 8 at 4 receiver locations. The results from the numerical methods seem to be in agreement with the analytic solution.

Figure 9 shows the errors using the two-norm and the max-norm for each numerical method. The error for each grid has been averaged over the whole frequency range of interest, *i.e.* from $f = 25$ Hz to $f = 1000$ Hz. Therefore, the convergence rate of second order is verified for the whole frequency range.

Both time and space discretization are tested. This case could be further extended to impedance boundary condition (not shown here). It could also be extended to long range sound propagation including meteorological effects [13] (not shown here).

4.5 Case 5 : plane wave scattering from a circular obstacle

4.5.1 Formulation

The monochromatic incident pressure p_i , propagating in the vicinity of a circular scatterer with a radius a , can be

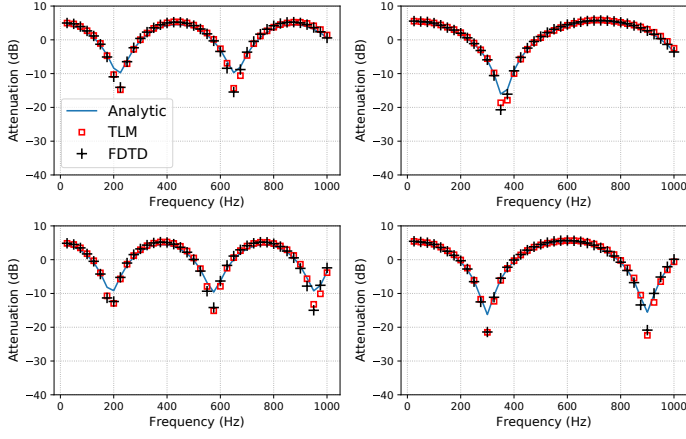


FIGURE 8 – Attenuation relative to free-field propagation for 4 receiver positions : from left to right, top to bottom, the coordinates expressed in meter ($x_1 = 1.28, y_1 = 0.96$); ($x_2 = 2.88, y_2 = 0.96$); ($x_3 = 4.80, y_3 = 0.96$); ($x_4 = 0.96, y_4 = 2.88$).

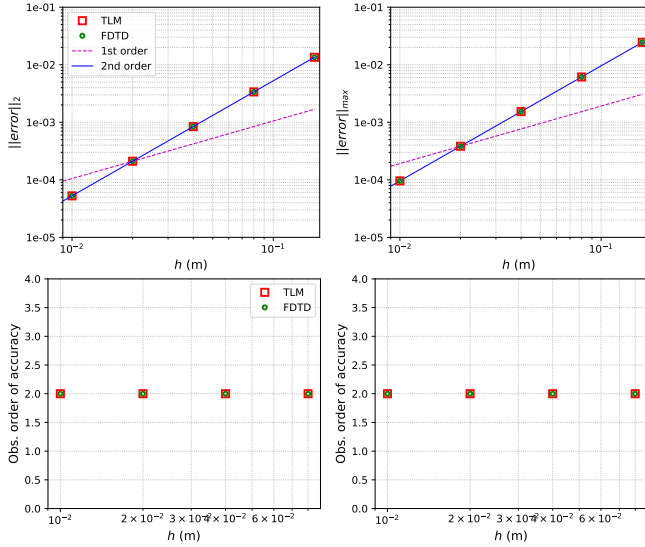


FIGURE 9 – Two-norm and max-norm of the absolute error (top) and the corresponding observed orders of accuracy (bottom) for case 4, using the FDTD and the TLM methods.

written in a cylindrical coordinate system (r, φ, z) as the sum of cylindrical waves as follows [14]

$$p_i = P_0 \sum_{m=0}^{\infty} (2 - \delta_{m0}) i^m J_m(kr) \cos(im\varphi) e^{i\omega t}, \quad (17)$$

where k is the wave number, ω the angular frequency, P_0 the amplitude of the incident wave, δ_{m0} the Dirac function and J_m the Bessel function of the first kind for real order m . The scattered wave is expressed as a divergent cylindrical wave as

$$p_s = P_0 \sum_{n=0}^{\infty} A_n H_n^{(1)}(kr) \cos(in\varphi) e^{i\omega t}, \quad (18)$$

where $H_n^{(1)}$ is the Hankel function of the first kind for real order n . The coefficients A_n are derived from the boundary condition, which can be written at $r = a$ as

$$\frac{i}{k\rho c} \frac{\partial}{\partial r} (p_i + p_s) = \frac{-1}{\beta} (p_i + p_s), \text{ for } r = a, \quad (19)$$

where β is the specific acoustic admittance [15] of the cylinder *i.e.* $\beta = \rho c / \gamma$, ρ is the mass density and c the sound speed in the air. The coefficients A_n are given by :

$$A_n = - \frac{(2 - \delta_{n0}) i^n [i J_n'(ka) + (\rho c / \beta) J_n(ka)]}{i H_n^{(1)'}(ka) + (\rho c / \beta) H_n^{(1)}(ka)}. \quad (20)$$

4.5.2 Numerical setup

As shown in Figure 10, the pulse emitted by the line source propagates from the left to the right of the domain, and is scattered by the circular obstacle located at the center of the domain.

The scatterer is located at the center of the computational domain and its radius is $a = 0.30$ m. The receivers are located on the 8 circles centered on the obstacle, with a radius ranging from 0.5 m to 4.0 m distance, every 0.5 m. All boundaries are considered as perfectly reflecting. The

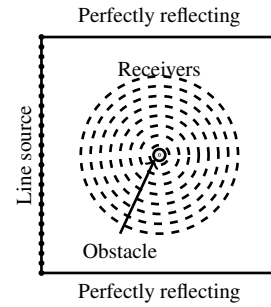


FIGURE 10 – Geometry of the numerical domain for the study of a pulse scattered by a circular obstacle.

simulations duration is set to not exceed 0.06 s, which is short enough to avoid any unwanted reflection at each receiver location.

The spatial steps for the 12 grids are $h = [0.0213, 0.0251, 0.0274, 0.0355, 0.0405, 0.0430, 0.0475, 0.0495, 0.0550, 0.0580, 0.0670, 0.0695]$ m, and the corresponding time steps T_s are set at the Courant limit for each grid.

4.5.3 Results

The pressure scattered around the obstacle recorded by the circle of receiver located at $r = 0.5$ m from the center is shown in Figure 11 for $f = 449$ Hz. The results obtained from the two numerical methods (TLM and FDTD) are in agreement with the analytic solution.

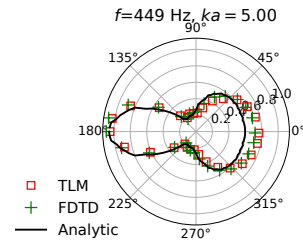


FIGURE 11 – Polar diagrams of the scattered field for $f = 449$ Hz calculated with the TLM, the FDTD and the analytic solution at the distance $r = 0.5$ m from the center of the scatterer.

Figure 12 shows the errors in two norms for the frequency $f = 449$ Hz. In this case, each frequency

requires a distinct fit in magnitude proportional to the analytic solution magnitude. Therefore, the error should be recalculated for each frequency. Although the global trend of the error approaches the second order of accuracy, it can be seen that the observed orders of accuracy is more fluctuating than for the previous cases. This can be explained by the normalization procedure of the magnitude for the numerical method that is applied for one chosen direction of incidence. A refined method for fitting the polar diagram might give smoother orders of accuracy.

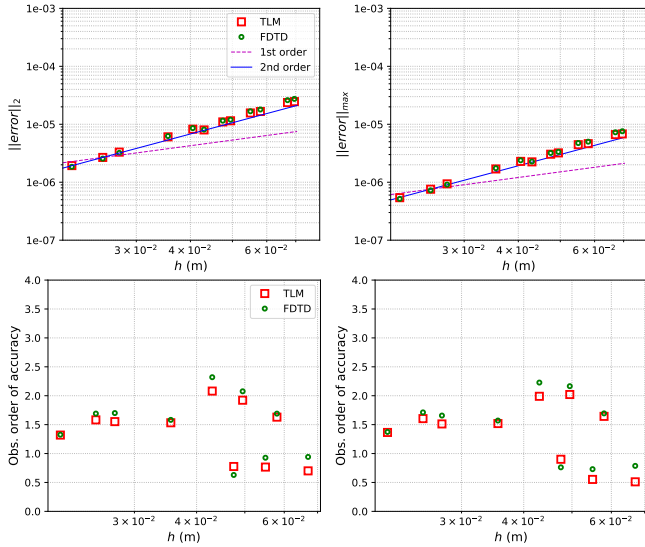


FIGURE 12 – Two-norm and max-norm of the absolute error (top) and their observed orders of accuracy (bottom) for case 5, with $f = 449$ Hz.

This case could be extended to impedance circular obstacles. This verification is only performed for a single frequency. However, it could be extended to a frequency range once the normalization procedure of the numerical signals would have been clarified.

5 Conclusion

The proposed verification procedure have been applied to five test cases, which have been implemented using two time domain methods (FDTD and TLM) and a frequency domain method (FDH). The expected second order convergence rate is returned by the codes for most cases. In order to complete this verification procedure, the observed order of accuracy should be calculated for a given frequency range and shown as a function of frequency. This would give the asymptotic range for which the code returns a verified results. As a general extension, test cases should also include 3D scenes. Finally, a validation procedure remains to be formulated using larger and more realistic cases that have been measured.

The code, its documentation and all related written documents are going to be available online, and will be open for contributions.

Acknowledgements

Thanks to Sebastian Prepelita from the Department of Computer Science, Aalto University, Espoo, Finland and

Simon Félix (LAUM, CNRS, Université du Mans, France) for the many fruitful discussions on this topic. Thanks to Le Mans Acoustique RFI for its financial support.

References

- [1] W. L. Oberkampf and T. G. Trucano. Verification and validation in computational fluid dynamics. *Progress in Aerospace Sciences*, 38(3) :209–272, Apr 2002.
- [2] W. L. Oberkampf and C. J. Roy. *Verification and Validation in Scientific Computing*. Cambridge University Press, 2010.
- [3] K. Attenborough, S. Taherzadeh, H. E. Bass, X. Di, R. Raspet, G. R. Becker, A. Güdesen, A. Chrestman, G. A. Daigle, A. L’Espérance, Y. Gabillet, K. E. Gilbert, Y. L. Li, M. J. White, P. Naz, J. M. Noble, and H. A. J. M. van Hoof. Benchmark cases for outdoor sound propagation models. *J. Acoust. Soc. Am.*, 1995.
- [4] M. Hornikx, M. Kaltenbacher, and S. Marburg. A platform for benchmark cases in computational acoustics. *Acta Acustica united with Acustica*, 101(4) :811–820, 2015.
- [5] R. J. LeVeque. *Finite Difference Methods for Ordinary and Partial Differential Equations : Steady-State and Time-Dependent Problems*. Society for Industrial and Applied Mathematics Philadelphia, 2007.
- [6] S. van der Walt, S. C. Colbert and G. Varoquaux. The NumPy Array : A Structure for Efficient Numerical Computation, *Computing in Science & Engineering*, 13, 22-30, 2011.
- [7] T. E. Oliphant. Python for Scientific Computing, *Computing in Science & Engineering*, 9, 10-20, 2007.
- [8] G. Hegedüs and M. Kuczmann. Calculation of the Numerical Solution of Two-dimensional Helmholtz Equation. *Acta Technica Jaurinensis*, 3(1) :75–86, 2010.
- [9] B. Hamilton and S. Bilbao. FDTD Methods for 3-D Room Acoustics Simulation With High-Order Accuracy in Space and Time. *IEEE/ACM Transactions on Audio, Speech and Language Processing (TASLP)*, 2017.
- [10] G. Guillaume, P. Aumond, B. Gauvreau, and G. Dutilleux. Application of the transmission line matrix method for outdoor sound propagation modelling - Part 1 : Model presentation and evaluation. *Applied Acoustics*, 76 :113–118, 2014.
- [11] P. Aumond, G. Guillaume, B. Gauvreau, C. Lac, V. Masson, and M. Berengier. Application of the Transmission Line Matrix method - Part 2 : Experimental validation using meteorological data derived from the meso-scale model Meso-NH. *Applied Acoustics*, 76 :107–112, 2014.
- [12] G. Sutmann. Compact finite difference schemes of sixth order for the helmholtz equation. *Journal of Computational and Applied Mathematics*, 203 :15–31, 2007.

- [13] M. C. Bérengier, B. Gauvreau, Ph. Blanc-Benon, and D. Juvé. Outdoor sound propagation : A short review on analytical and numerical approaches. *Acta Acustica united with Acustica*, 89(6) :980–991, 2003.
- [14] M. Bruneau. *Fundamentals of Acoustics*. Wiley-Blackwell, Jan 2006.
- [15] P. Morse, K. Ingard, *Theoretical acoustics*, Princeton University Press, 1987.